Wu *et al. Geoscience Letters* (2024) 11:37
https://doi.org/10.1186/s40562-024-00354-6

Geoscience Letters

RESEARCH LETTER

Open Access

Seismogenic structures along the deformation front from onshore to offshore SW Taiwan

Wen-Nan Wu[1*], Jing-Yi Lin[1], Wen-Bin Doo[2], Chung-Liang Lo[1] and Shu-Kun Hsu[1]

Abstract

Accurately imaging seismogenic structures is crucial for seismic hazard assessment. This is especially important around the deformation front (DF) region off SW Taiwan, where seismic potential is high but the fault structure and seismic activity are still poorly understood. Here, we present a comprehensive delineation of seismogenic structures along the onshore and offshore DF of SW Taiwan, utilizing hypocenter relocations and first-motion focal mechanism solutions from January 1991 to March 2019. Five distinctive seismogenic structures are delineated. Particularly, the energetic seismic activity initialled after the 2017 Mw5.3 Tainan earthquake and migrated northeastward along the western side of the DF. The offshore trace of the DF could serve as a boundary delimiting the seismic activity driven by the flexural stress of the subducted Eurasia Plate to the west of the DF. This observation could constrain the magnitude estimation of future earthquakes offshore SW Taiwan. Meanwhile, the areas with higher seismic moment release are located near the DF rather than known faults, indicating that the DF may dominate the seismic moment release. However, further study is warranted into the intricate relationship among seismic strain variation, the structure of DF, and seismic activity to further understand the seismic potential. Our first-motion focal mechanism solutions show that several earthquakes in SW Taiwan were characterized by *P*-axis orientations parallel to the strike of the Taiwan orogeny. Those events are preferably explained by the lateral compression induced by the ongoing collision between the Eurasia and Philippine Sea plates.

Key Points

- The deformation front has high seismic potential but seismogenic structure remains unclear.
- The deformation front confined seismic activity and released relatively large seismic moments.
- The role of the deformation front must be considered in seismic hazard assessment.

Keywords Manila Trench, Taiwan orogeny, Deformation front, Seismogenic structure, Seismic hazard assessment

Introduction

Taiwan, located within an active convergent orogenic belt, results from the collision between the Eurasia Plate (EP) and the Philippine Sea Plate (PSP). In southern Taiwan, the EP subducts beneath the PSP along the Manila Trench, while in NE Taiwan, the PSP subducts under the EP along the Ryukyu Trench. This convergence, driven by

*Correspondence:
Wen-Nan Wu
wennan.v.wu@gmail.com
[1] Department of Earth Sciences, National Central University, Taoyuan, Taiwan
[2] Center for Environmental Studies, National Central University, Taoyuan, Taiwan

about 80 mm/year of northwestward motion of the PSP relative to the EP (e.g., Tsai et al. 2015b; Yu et al. 1997), leads to frequent disastrous earthquakes (Fig. 1a). It is obvious that seismic activity is more pronounced off NE Taiwan. Previous studies have suggested the potential for a large (Mw ≥ 7.5) earthquake in NE Taiwan (Hsu et al. 2012; Chen et al. 2022). In contrast, the seismogenic structure off SW Taiwan, particularly in areas near the deformation front (DF) that marks the front limit of the Taiwan orogen's fold-and-thrust belt (Liu et al. 1997; Yang et al. 2016; Yu 2004), has received relatively less attention due to its historically lower seismicity. Remarkably, no recorded earthquakes with M > 5 occurred off SW Taiwan during the period from January 1991 to February 2017 (Fig. 1b). Nonetheless, previous studies (e.g., Wu et al. 2021) have demonstrated the potential for significant seismic hazards offshore SW Taiwan.

In particular, a series of low-to-moderate magnitude earthquakes have successively occurred near the western boundary of the DF since the Tainan earthquake on 10 February 2017, with hypocenter parameters cataloged by the Central Weather Administration (CWA) of Taiwan: 17:12:52.56 UTC, $M_L = 5.71$, 22.8657°N, 120.1432°E, at a depth of 16.15 km (Fig. 1c), hereinafter referred to as the 2017 Tainan earthquake. This unusual progression in seismic activity raises questions and suggests a complex interplay of tectonic stress and local tectonics. Recently, Wu et al. (2021) used joint travel time data from a temporal deployment of ocean-bottom seismometers and permanent inland seismographs to relocate 2 week worth of aftershocks following the 2017 Tainan earthquake. Their findings indicated that most aftershocks form an NE–SW striking seismogenic structure approximately parallel to the surface trace of the DF, unlinked to any known faults in SW Taiwan. In addition, they identified a conjugate fault system comprising an SW-dipping NE–SW striking fault and an SE-dipping NW–SE striking fault. However, it is important to note that these aftershocks occurred within a short time frame after the mainshock, which likely predominantly represented the main characteristics of the mainshock's rupture, lacking detailed insights into the pre- and post-seismic evolution and seismogenic structure of fault slip. Of particular interest is the remarkable increase in seismic activity along the DF following the 2017 Tainan earthquake (Fig. 1c).

In this study, we comprehensively analyze relocated hypocenters and P-wave first-motion focal mechanisms catalogs spanning about three decades to explore the spatiotemporal evolution in seismogenic processes and associated deformation patterns along the DF from offshore to onshore. This long-term perspective allows us to understand better and characterize seismogenic structures in our study area. Most importantly, mapping the distribution of newly occurred events may unveil previously unrecognized seismogenic characteristics, which is crucial for seismic hazard assessment.

Data and methods

Travel time and first-motion polarity data

Our analysis relies on P- and S-wave arrival times and P-wave first-motion polarity data from the CWA of Taiwan earthquake bulletin. We use data from January 1991 to March 2019, excluding ocean bottom seismometer data analyzed by Wu et al. (2021) to mitigate short-term bias in earthquake relocation from variations in network geometry and station density. The accuracy of hypocenter locations relies heavily on station distribution. Due to the absence of long-term ocean-bottom seismometers, we rely on seismic stations on the Penghu Islands to improve location accuracy off SW Taiwan. Data from Penghu dating back to 2002 and CWA equipment upgrades in 2012 have improved earthquake detection. Seismic ray paths between events and stations confirm good station coverage near the southwestern coast (Fig. S1), validating the data set's suitability for our study objectives.

Absolute hypocenter relocation and optimal 1-D velocity models

We adopt an earthquake relocation scheme following Wu et al. (2021), which consists of two steps to obtain reliable spatiotemporal distribution of seismicity. First, we simultaneously invert absolute hypocenter locations and 1-D P- and S-wave velocity models using the VELEST program (Kissling et al. 1994; Lin 2013). These inverted optimal models are then used for relative hypocenter relocations employing the shrinking box source-specific

(See figure on next page.)

Fig. 1 Tectonic background and distribution of the seismic stations and earthquakes. **a** Tectonic setting of the Taiwan mountain belt. Topography/bathymetry data of the region comes from version 25.1 of the global marine bathymetry database (Sandwell and Smith 1997). An open arrow denotes the direction of plate motion of the Philippine Sea Plate relative to the Eurasia Plate (Tsai et al. 2015a; Yu et al. 1997). Our study area is delineated by the box. Open circles represent hazardous earthquakes occurring between 1900 and 2022, as reported by the Central Weather Administration (CWA) of Taiwan (https://scweb.cwa.gov.tw/zh-tw/page/disaster). Triangles represent seismic stations, and all are used in this study. DF is the deformation front. The distribution of seismicity used for analysis in this study, indicated by solid circles, is shown both before (from January 1991 to February 2017) and after (from February 2017 to March 2019) the 10th February 2017 Tainan earthquake (a star) in (**b**) and (**c**), respectively. The minimum magnitude of the used earthquakes is 0.5

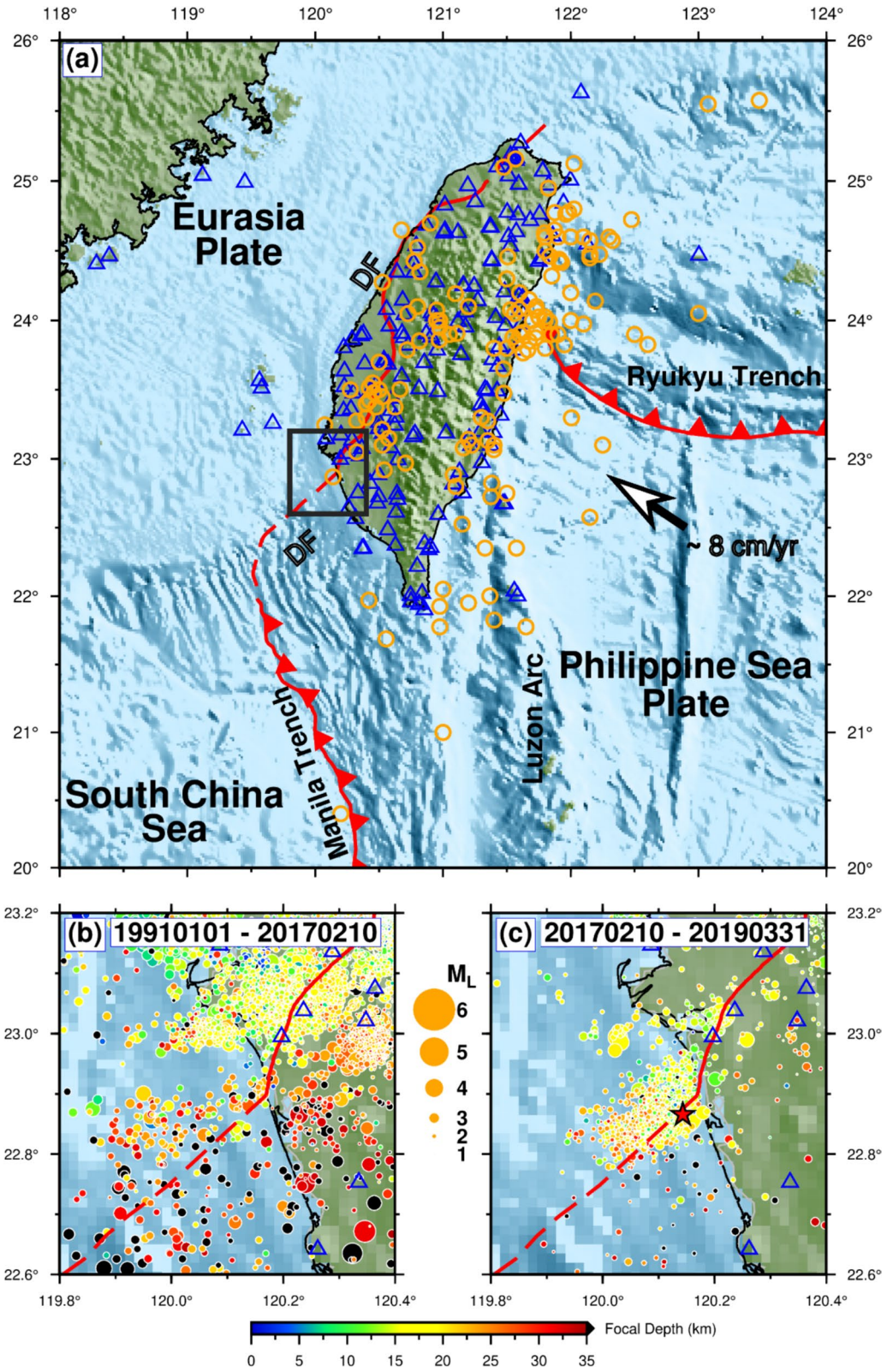

Fig. 1 (See legend on previous page.)

station term (SSST) method (Lin 2018; Lin and Shearer 2005).

Since seismic station density and data quality of the CWA increase with time, we slightly revised our earthquake relocation scheme for taking care of data with relatively less constraint, as follows. First, we select the well-constrained events and use them to simultaneously determine optimal Vp and Vs 1-D velocity models as well as absolute hypocenter locations with minimum root mean square (RMS) of the travel time residual using the VELEST program. Then, these optimal velocity models are used to relocate absolute hypocenter locations of the rest of events (less-constrained events) in our data set. Finally, we perform relative hypocenter relocation for all events by using the shrinking-box SSST method. In this way, we can obtain the velocity models without being polluted by the relatively less-constrained travel time data and thus ensure reliable velocity models and hypocenter locations.

The well-constrained events are defined as having at least four P- and four S-arrivals with level ≤ 2 (level 0 means best and level 4 means worst) as well as an azimuth gap angle of $\leq 180°$. The rest of the earthquakes in the routine catalog are defined as less-constrained events. We have 1186 well-constrained events and 2888 less-constrained events for the analysis. The well-constrained events contributed 416,828 P-wave arrivals and 271,523 S-wave arrivals, and the less-constrained events yielded 748,422 P-wave arrivals and 520,231 S-wave arrivals.

To obtain an appropriate 1-D reference velocity model, we follow a flowchart by Wu et al. (2021) to first test different initial 1-D velocity models from the CWA 1-D velocity model (Chen and Shin 1998), average 1-D velocity models extracted from 3-D velocity models of Kuo-Chen et al. (2012) (Kuo-Chen 1-D model) and Huang et al. (2014) (Huang 1-D model). We found that the inversion result of the CWA 1-D velocity model has a smaller RMS (0.431 s) than the Kuo-Chen 1-D model (0.543 s) and Huang 1-D model (0.436 s) based on the data set of the well-constrained events. Thus, we use the CWA 1-D Vp and Vs velocity models as the reference velocity model. To further reduce the effect of the reference velocity model on the inversion result (e.g., Wu et al. 2021; Wang et al. 2019; Hicks et al. 2014), we generate 2000 initial velocity models by randomly perturbing $\pm 5\%$ of each layer of the 1-D Vp and Vs CWA velocity models (Fig. 2a).

From these, we obtained 2000 sets of inverted velocity models, hypocenter locations, and RMS travel time residuals by performing the VELEST program. Averaging the RMS travel time residuals from these sets provided us with the mean RMS (0.446 s) and a standard deviation (0.035 s) (Fig. 2b). We identified 319 optimal solutions by selecting sets with an RMS travel time residual lower than the mean minus one standard deviation. These solutions comprised 319 optimal velocity models (Fig. 2c) and 319 corresponding hypocenter locations for each earthquake. The distribution of 4074 events located by the CWA is shown in Fig. 3a. We further determined the optimal relocated location for each earthquake by averaging the hypocenter locations from these sets and calculated the location error as the standard deviation of distances between individual hypocenter locations and the averaged hypocenter location. The absolute hypocenter location is referred to as the VELEST relocation result (Fig. 3b). Subsequently, the 319 optimal velocity models have been utilized for hypocenter relative relocation with the shrinking-box SSST method, yielding another 319 sets of relative relocation results. Similar to the VELEST stage, we averaged the hypocenter locations from these sets to obtain the optimal relative hypocenter relocation result and the corresponding location error, namely the SSST result (Fig. 3c).

Our inverted optimal velocity models show a relatively low-velocity upper crust compared to the 1-D velocity model provided by the CWA. Within the study area, numerous mud diapirs and mud volcanoes have been observed (e.g., Doo et al. 2015; Chen et al. 2014), potentially linked to the low velocities we have inferred. However, as noted in the previous study (Wu et al. 2021), the 1-D velocity structure represents an average model of ray paths between events and stations. To gain a clearer insight into the origins of the low-velocity layer, a more detailed and high-resolution 3-D velocity model is essential. Besides, the velocity reduction in the upper crust is significantly slower than the model from Wu et al. (2021). This could be because the previous study only focused on 2 weeks, and these earthquakes were concentrated in the source area of the 2017 Tainan earthquake. In contrast, the current data spans a longer period and originates from a wider range of earthquake locations.

Relative hypocenter relocation

It is crucial to highlight that during the shrinking-box SSST relocation processes, each event's updated hypocenter location is influenced by other events (Lin and Shearer 2005). To reduce the effect of less-constrained events on the overall relocation result, we modified the shrinking-box SSST program to take the quality of travel time readings as a weighting factor. The lower reading quality is assigned a lower weight in the relocation processes. Furthermore, after a set of experiments with different values of the control parameters (e.g., Wu et al. 2021) (Table S1), we determine optimal control parameter values to obtain the result with a smaller error (0.255 ± 0.001 s). When comparing the aftershock

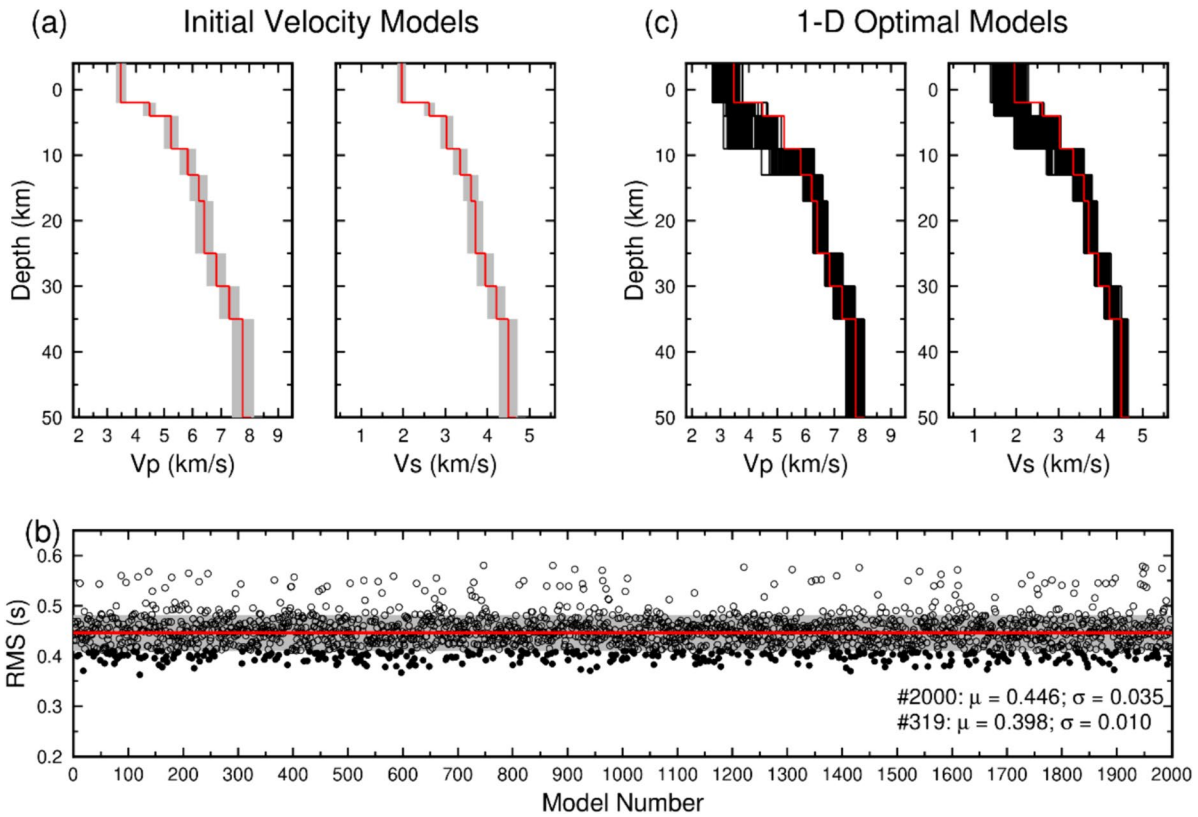

Fig. 2 **a** Initial 2000 bootstrap resamples (gray lines) of 1-D *P*- (left panel) and *S*-wave (right panel) velocity models used for inversion. These models were constructed with a variability of ± 5% relative to the CWA 1-D *P*- and *S*-wave reference velocity models. **b** Presentation of the room-mean square (RMS) travel time residuals associated with the initial velocity models. The red solid line represents the mean value (0.446 s) of the RMS travel time residual, and the gray band indicates the confidential interval within one standard derivation (0.035 s). Black solid circles are the optimal velocity models where the RMS travel time residuals fall below the mean RMS value minus one standard derivation. **c** Inverted *P*-wave (left panel) and *S*-wave (right panel) velocity models are represented by black lines, based on the optimal velocity models. Red lines in (**a**) and (**c**) are the *P*-wave (left panel) and *S*-wave (right panel) of the CWA 1-D reference velocity models

hypocenter relocation locations of the 2017 Tainan earthquake with the constraints from ocean-bottom seismometers (Wu et al. 2021) (Fig. S2), the overall earthquake distribution patterns are similar. However, the earthquakes with ocean-bottom seismometer constraints show a more concentrated distribution of hypocenters. We also observed an anomalously deep location for a less-constrained event, highlighting the importance of constraints provided by ocean-bottom seismometers in relocating offshore earthquakes.

First-motion focal mechanism determination

We determine focal mechanism solutions by applying the HASH software (Hardebeck and Shearer 2003) to P-wave first-motion polarity data. The first-motion focal mechanism solution is computed via a grid search perturbating the ray azimuth and take-off angle with a resolution of 5°. The quality of the first-motion focal mechanism solution is dependent on the reliability of first-motion readings, earthquake locations, and seismic velocity models (Hardebeck and Shearer 2003; Kilb and Hardebeck 2006). To enhance the reliability of our focal mechanism solutions by minimizing the influence of event location and velocity model uncertainties, we first use events satisfying the following selection criteria, such as the number of P-wave first-motion polarities exceeding eight, maximum source-to-station azimuth gap less than 90°, and maximum take-off angle gap less than 60° (e.g., Lin and Okubo 2016). Then, for each used event we compute the ray azimuth and take-off angle from the shrinking-box SSST relative hypocenter location with 319 optimal P-wave velocity models. The HASH software computes a set of acceptable mechanisms for each event and classifies the quality from A to E in decreasing quality based on the probability, RMS fault plane uncertainty, average misfit, and station distribution ratio (Hardebeck and Shearer 2003). We use the default values in the HASH program to evaluate the quality of the focal mechanism solution. Finally, when multiple acceptable solutions exist for a given event, the one with the highest quality is selected.

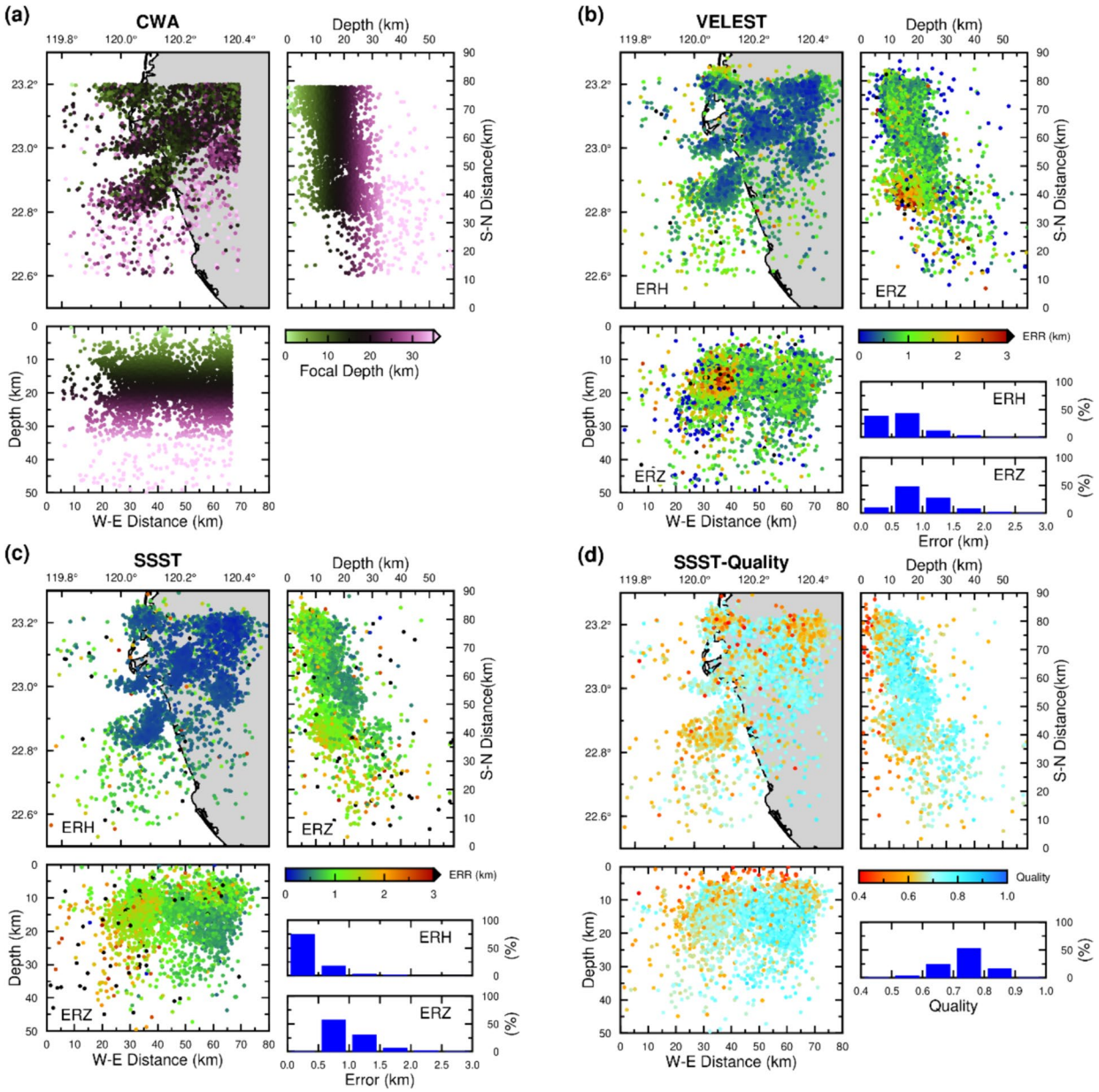

Fig. 3 **a** Distribution of seismicity reported by the CWA. **b** Distribution of relocated seismicity by the VELEST software is represented by solid circles scaled with colors, along with statistical errors in depth (ERZ) and horizontal (ERH). **c** Similar to Fig. 3a, this panel displays the inversion results obtained using the shrinking box source-specific station term (SSST) method. **d** Relocation quality assessment for the shrinking box SSST method (Text S1). Approximately 99% of the location quality measurements exceed 0.5, with the majority falling within the range of 0.7–0.8. Instances of poorer location quality primarily result from factors such as a limited number of seismic stations available for early events or their offshore locations, which pose challenges for precise localization

In total, we have obtained first-motion focal mechanism solutions for 441 earthquakes, categorized as 21 quality A, 35 quality B, 36 quality C, and 349 quality D. To ensure accurate tectonic interpretation, only events with quality A and B (the average polarity error < 0.2°, the root-mean-square uncertainty in the fault plane solution < 35°, station distribution ratio > 0.4, and the mechanism probability > 0.6.) were used for interpretation (Table S2 and Fig. S3).

Results and discussion

Relocation uncertainty and quality

Our relocation results, along with associated errors from the VELEST and shrinking-box SSST methods, are

presented in Fig. 3b, and c. We further classify relocation quality (Text S1) on a scale from 0.0 to 1.0, with increasing values indicating higher quality. This classification considers azimuth gap angles, the number and quality of P- and S-phase readings, distance to the closest station, and the RMS of the travel time residual (e.g., Husen and Hardebeck 2011). The value of quality ranges from 0.40 to 0.92, and a predominant concentration is between 0.7 and 0.8 (Fig. 3d).

Seismogenic structures revealed by relocated seismicity and focal mechanisms

Based on the spatiotemporal pattern of the shrinking-box SSST relocated hypocenters and focal mechanism solutions (Figs. 4 and 5), we delineate five distinct seismogenic zones, labeled A, B, C, D, and E (Fig. 4). Each of these zones exhibits unique seismic activity patterns and deformation characteristics.

Zone A situated in the northwestern periphery of the study area and displays significant seismic activity, particularly during the period from 1991 to 1999 (Figs. 4a–c and S4a). Subsequently, seismicity conspicuously declined after 2005 but was resurgent in 2017 (Fig. S4a). In this area, earthquakes tend to manifest at depths shallower than 15 km (Fig. 5a, d), and their genesis is intrinsically linked to the 12 March 1991 Chiali earthquake (CWA catalog hypocenter parameters: 06:04:06.14 UTC, $M_L = 5.67$, 23.2457°N, 120.0745°E, 12.26 km) (Figs. 4a–c). We must point out that the Chiali earthquake, which falls beyond the spatial boundaries of our current study, serves as a foundational event in comprehending the seismic activity of Zone A. Nevertheless, the exhaustive examination of the Chiali earthquake sequence is beyond the scope of the present study. Due to the limited data set consisting of only two high-quality focal mechanism solutions available (Fig. 5b, d), it is not appropriate to make definitive inferences regarding the tectonic deformation pattern in this area.

Zone B encompasses the inland segment of the DF and is characterized by pronounced seismic activity observed throughout our study period (Figs. 4, S4b, and S5.) Within this region, seismicity is widespread throughout the entire crust, with a marked concentration of earthquakes primarily occurring at depth ranges of 10–20 km (Fig. 5). The focal mechanism solutions for the majority of these events are typified by strike-slip faulting (Fig. 5a, d and g), while certain instances of normal faulting and thrust faulting earthquakes with discernible strike-slip components (Fig. 5e, f and h). Upon analysis of the fault orientations derived from these strike-slip earthquakes, coupled with the spatial distribution patterns of the relocated events, it becomes apparent that a complex conjugate fault system exists, exhibiting orientations both in the NE–SW and NW–SE directions. However, based on visual examination, the distinct definition of a specific conjugate fault system remains challenging, necessitating further evidence for conclusive determinations. Employing the matching filtered technique (e.g., Essing and Poli 2022; Chamberlain et al. 2021) or artificial intelligence algorithms (e.g., Mousavi et al. 2020; Zhu et al. 2023) or both for the detection of smaller earthquakes holds promise for enhancing our ability to identify the conjugate fault system, and this will be a central focus of our forthcoming research efforts.

Zone C had experienced minimal seismic activity before the 6 February 2016 Meinong earthquake, documented in the CWA catalog with hypocenter parameters as follows: 19:57:26.08 UTC, $M_L = 6.60$, 22.922°E, 120.5438°N, 14.64 km (Figs. 4a–i and S4c). While the Meinong earthquake fell outside our study area, seismic activity within **Zone C** surged immediately following the Meinong earthquake and subsequently subsided (Figs. 4i–k and S4c). Consequently, a significant proportion of these events could be categorized as the Meinong earthquake aftershocks. Most of the earthquakes in this region occurred at depths ranging from 15 to 40 km and are characterized predominantly by strike-slip faulting mechanisms (Fig. 5). Furthermore, as shown in Fig. 5j, there are four earthquakes (events 35, 36, 38 and 40) wherein the orientation of the *P*-axes aligns parallel to the strike of the Taiwan orogeny, exhibiting an NE–SW trending pattern. Similar events also were found in other subareas (events 2, 12, 32, 43, 46 and 54; Fig. 5a, d and g). These earthquakes are characterized by smaller magnitudes (M_L), ranging from 2.9 to 4.6, with depths ranging from 7.6 to 23.1 km, distributed throughout the entire crust. Such kinds of events have also been reported in the study of the 2010 Jiashian earthquake sequence in southern Taiwan by Rau et al. (2012). Due to the distribution of events across various regions and different periods, it is reasonable to ascribe these events to reflect the collision between the PSP and EP (e.g., Rau et al. 2012; Kao et al. 1998). This finding provides additional evidence to demonstrate that the southern region of Taiwan, where the collision has just commenced (Huang et al. 1997, 2000), has already experienced the lateral compression induced by the collision.

Zone D occupies a significant position within the advanced collision region (Huang et al. 1997, 2000), where seismic activity has exhibited a heightened level of activity (Fig. S4d). The hypocenters in this zone have predominantly clustered within a depth range of 10–20 km (Fig. 5). Furthermore, the prevailing faulting type for these events is largely characterized by normal faulting (Fig. 5f, g), which may be intricately linked to the flexural bending of the subducted EP (e.g., Wu et al. 2021).

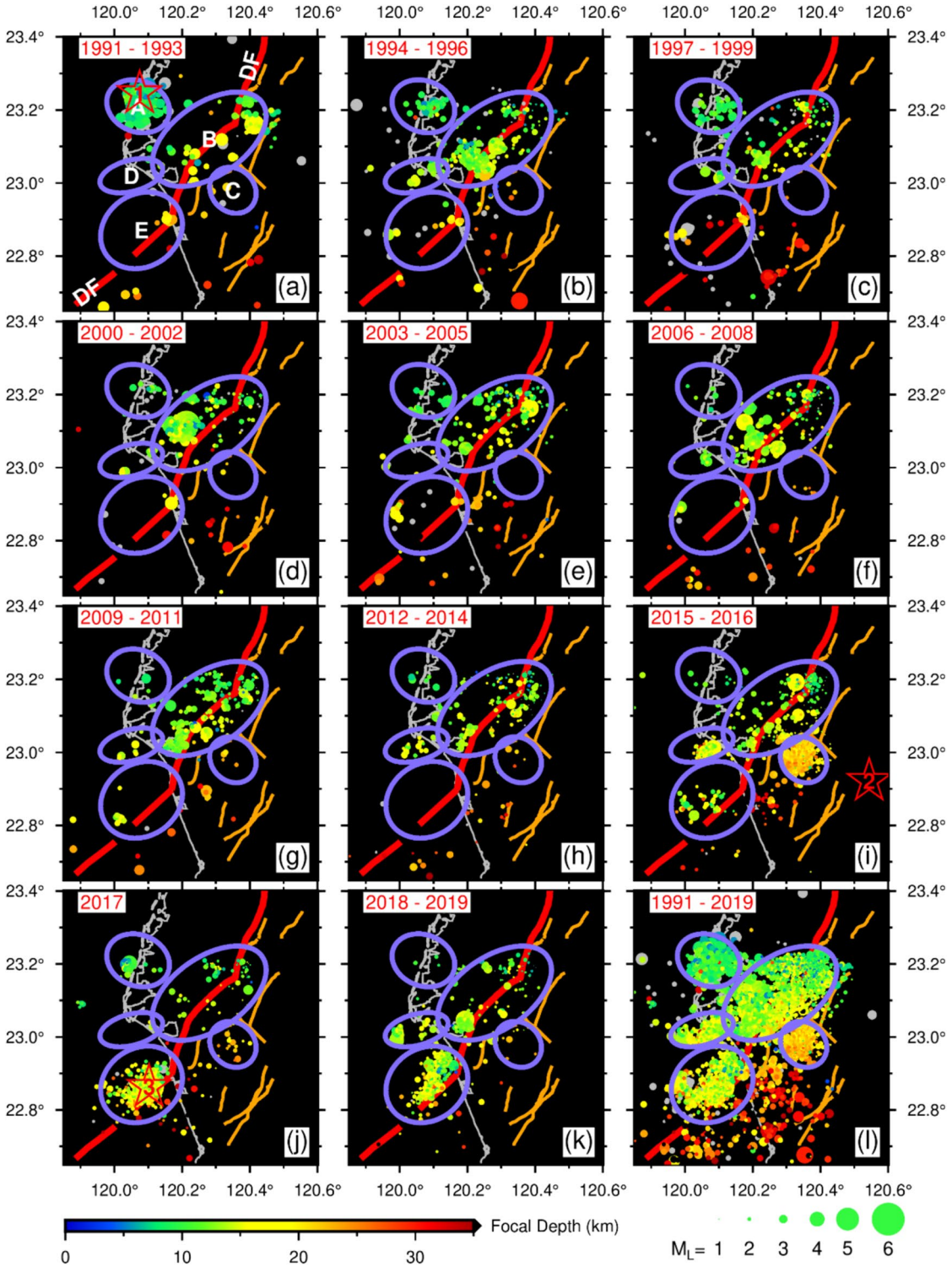

Fig. 4 **a**–**k** Spatiotemporal distribution of relocated seismicity using the shrinking-box SSST method across different periods indicated by the numbers at the top of each panel. l Distribution of all earthquakes during the study period. Five distinct seismogenic zones **A**–**E** (ellipses outlined with purple color) are defined. Seismic events with a relocation quality score of ≥ 0.6 are represented by colored circles, while those with a relocation quality score of < 0.6 are shown as gray circles. Known fault lines, as reported by Lin et al. (2021), are depicted by orange thin lines, with the DF denoting the deformation front. Open star 1 in (**a**) represents the 1991 Chiali earthquake; open star 2 in (**i**) marks the 2016 Meinong earthquake; open star 3 in (**j**) denotes the 2017 Tainan earthquake

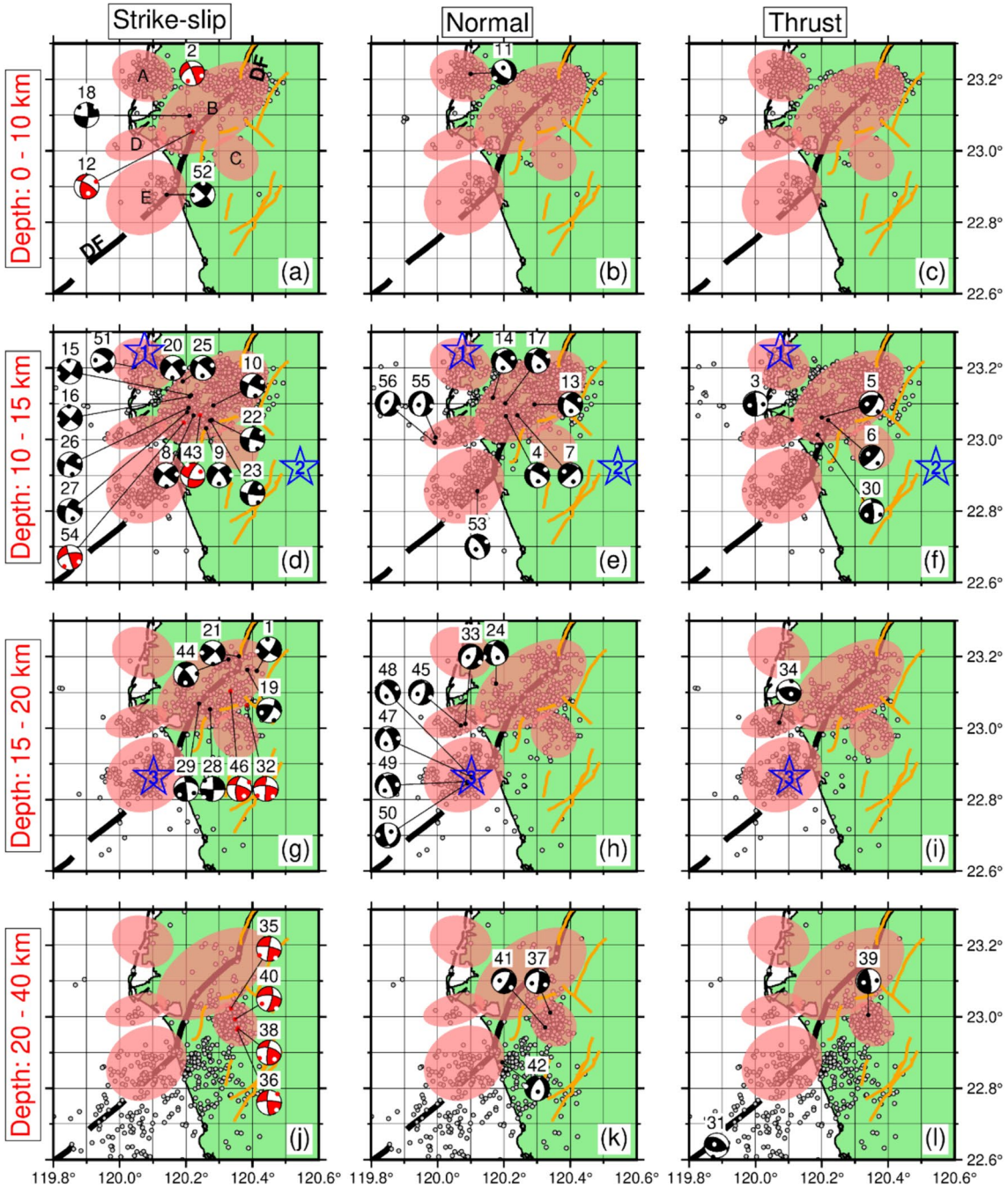

Fig. 5 Spatial distribution of our relocated seismicity by the shrinking-box SSST method and first-motion focal mechanism solutions determined by the HASH algorithm. Strike-slip events with relocated seismicity at 0-10 km (**a**), 10-15 km (**d**), 15-20 km (**g**), 20-40 km (**j**); normal faulting at 0-10 km (**b**), 10-15 km (**e**), 15-20 km (**h**), 20-40 km (**k**); thrust faulting at 0-10 km (**c**), 10-15 km (**f**), 15-20 km (**i**), 20-40 km (**l**). Only earthquakes with a relocation quality score of ≥ 0.6 are depicted as opened circles. The focal mechanisms are displayed in a lower-hemisphere projection. Symbols are the same as that in Fig. 4. Red lower-hemisphere projections represent earthquakes with NE–SW oriented *P*-axis; black ones denote other orientations. Dots indicate *P*-axis (black or red) and *T*-axis (white)

Zone E, corresponds to the focal area of the 2017 Tainan earthquake sequence, which is within the outer-rise region (Wu et al. 2021). Before September 2015, this area was characterized by a scarcity of seismic events (Figs. 4a–h and S4e). Following the 2017 Tainan earthquake, seismic activity remarkably increased and

migrated in a northeastward direction, progressing toward the coast of SW Taiwan along the western side of the DF surface trace (Figs. 4i–k and S6–9). These earthquakes were spread out across the crust, with most of them occurring in the depth range of 10–40 km (Fig. 5). Focal mechanism solutions exhibit a combination of normal faulting with strike-slip components (Fig. 5a, e and h), which is attributed to the flexural bending of subducted EP (Wu et al. 2021). Based on these observations, it seems reasonable to suggest that the offshore trace of the DF may act as a boundary, marking an area to the west where seismic activity is primarily induced by the flexural stress of the subducted EP. In this case, we may further determine the bending moment of the subducted slab (e.g., Sandiford and Craig 2023) and estimate the maximum magnitude of potential earthquakes that may occur within this region. Moreover, regarding our observation of northeastward migration of seismic activity along the western flank of the DF, previous studies have frequently associated such seismic migrations with fluid processes or post-seismic slip (e.g., Ross et al. 2017; Hatch et al. 2020). The mechanism underlying this seismicity migration along the DF falls beyond the scope of this study and will be explored in detail in our upcoming research. In addition, the absence of well-constrained thrust-faulting focal mechanism solutions makes it hard to characterize the interplate thrust zone off SW Taiwan, implying a relatively low degree of interplate coupling within this region (e.g., Lo et al. 2017).

Spatiotemporal distribution of cumulative seismic moment release

Since the seismic moment is physically clear and related to seismic strain release (e.g., Chen et al. 2012; Wu et al. 2017; Lin and Wu 2012), we further determined the spatiotemporal distribution of the cumulative seismic moment release to provide an alternative perspective of seismic activity. In practice, we began by converting the local magnitude (M_L) of the shrinking-box SSST relocation events to seismic moment (M_0 in dyne-cm) through the two empirical relations: $Mw = 0.87M_L + 0.23$ (Jian et al. 2018) and $\log M_0 = 1.5Mw + 16.1$ (Hanks and Kanamori 1979). Subsequently, we divided the study area into grid nodes spaced at 0.05° apart and calculated the cumulative seismic moment encompassing all events within a $0.05° \times 0.05°$ rectangle centered at each node for different periods. As displayed in Fig. 6, the regions with comparatively high seismic moment release are predominantly near the surface trace of the DF. Notably, two subareas, which are distant from the DF, exhibit significant seismic moment release. One of these subareas links to the 1991 Chaili earthquake (Fig. 6a), while the other is associated with the 2016 Meinong earthquake (Fig. 6i). These observations highlight the heterogeneous distribution of seismic strain release within the study area.

One of the striking features in the seismic moment release pattern is that Zone B has repeating energy bursts (Figs. 6, S4b, and S5). During three significant periods of high cumulative seismic moment release (1994–1996, 2000–2002, and 2006–2008) in Zone B, events were primarily associated with strike-slip faulting (Fig. 5b, d and f). As shown in Fig. S5, between 1994 and 1996, two seismic swarm sequences were identified in 1995 and 1996, characterized by multiple earthquakes with similar magnitudes ranging between 4.0 and 4.5, indicating earthquake swarm sequences (Vidale and Shearer 2006). From 2000 to 2002, the largest earthquake occurred toward the end of 2000, followed by a rapid decrease in earthquake magnitudes, indicative of a mainshock and aftershock sequence. Similarly, the earthquakes observed in 2006 within the 2006–2008 period also displayed characteristics of a main- and after-shock sequence. These findings highlight the complex nature of seismicity in the region. The complexity arises from the varying patterns of earthquake occurrences, including both swarm sequences and mainshock–aftershock sequences, which suggest different triggering mechanisms and fault interactions. This variation in seismic behavior points to a more intricate and dynamic tectonic environment than a region exhibiting a single type of seismic activity. Therefore further comprehensive investigations into the underlying mechanisms are necessary to fully understand these seismic complexities.

It is important to emphasize that the areas near the surface trace of the DF release a higher seismic moment release when compared to known faults reported by the Geological Survey and Ming Management Agency, Ministry of Economic Affairs, Taiwan (Lin et al. 2021). However, this disparity does not necessarily imply a reduced seismic hazard potential for active faults. There is a plausible scenario in which the active faults in SW Taiwan progressively accumulate strain energy without substantial release during our study period, potentially resulting in an elevated seismic threat. Besides, for the observation of the DF exhibiting a higher seismic energy release, on one hand, higher strain release might hint at its ongoing activity and the potential for a large earthquake. On the other hand, it could also signify that the stress in the area has been gradually diffusing over time, reducing the potential for a large rupture. This ambiguity highlights the intricacies and uncertainties that surround seismic risk assessment, particularly in areas prone to tectonic activity. Given these uncertainties, caution is imperative when dealing with active fault zones. Furthermore, note that in this study the delineation of the inland surface trace of the DF in SW Taiwan is based on the endpoints

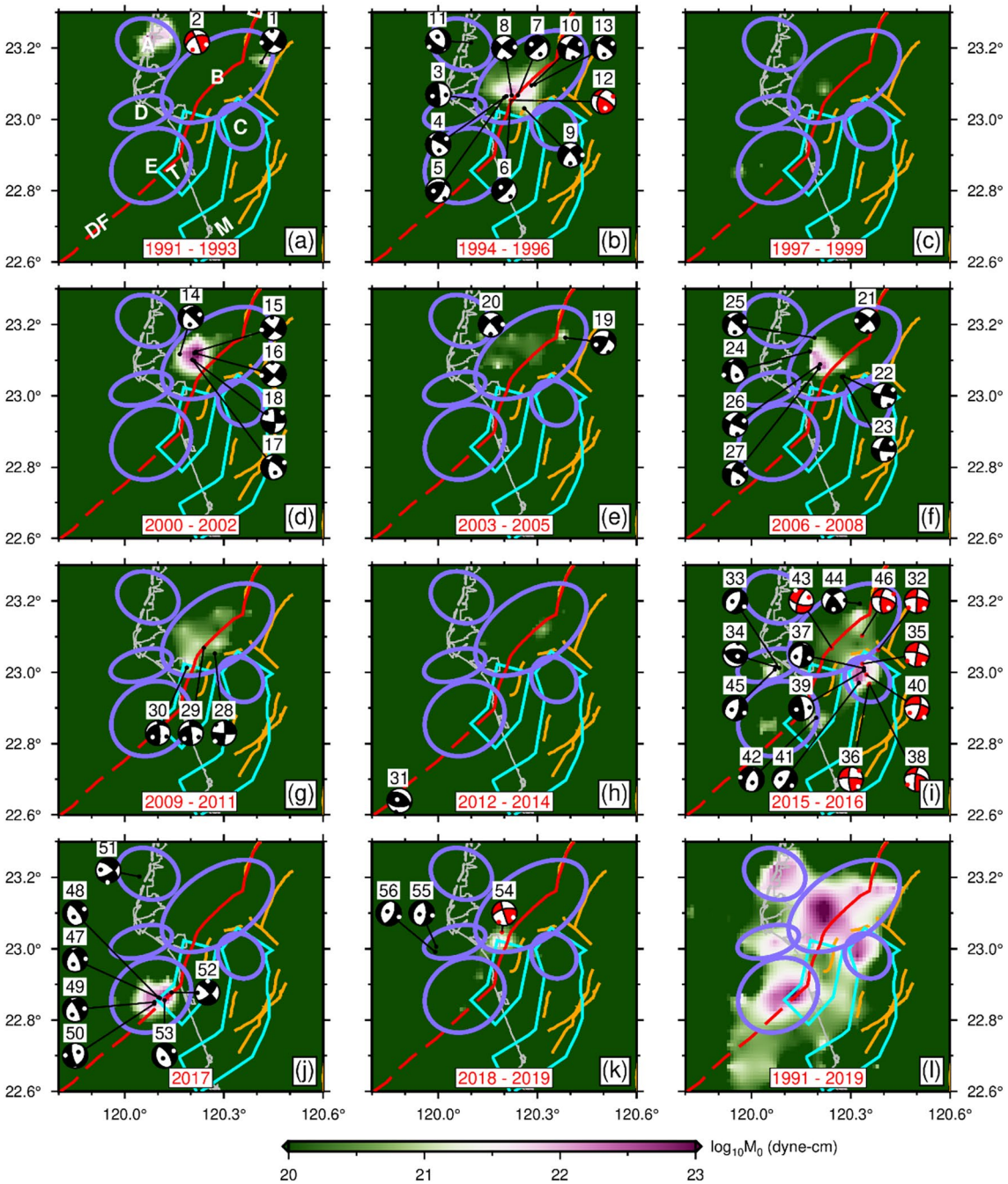

Fig. 6 **a**–**k** Spatiotemporal distribution of cumulative seismic moment release with focal mechanism solutions across different periods indicated by the numbers at the bottom of each panel. **l** Spatial variation in the total cumulative seismic moment release for the entire study period. Symbols are the same as that in Figs. 4. Two blocks outlined by cyan lines that were defined by Ching et al. (2011) are the Tainan Fault Block (T) and the Meilin Fault Block (M), respectively

of a series of westward-dipping ramp anticlines (Liu et al. 1997), rather than active faults. Thus, understanding the mechanisms behind the DF's (anticlines) enhanced earthquake moment release and its impact on stress patterns in the surrounding areas is important. This knowledge contributes to a comprehensive understanding of the dynamics of the fault system and aids in the evaluation of potential future seismic events. Therefore, it is crucial to incorporate the DF into future seismic hazard assessment models.

In addition, Ching et al. (2011) conducted simulations of the Tainan Fault and Meilin Fault block movements and found that the Tainan Fault and Meilin Fault exhibit significant slip rate deficits of 18.8 mm/yr and 33.9 mm/yr, respectively. This indicates that the slip rates on these fault lines are much lower than expected, suggesting incomplete release of geological strain. The Tainan Fault block encompasses the DF transitioning from offshore to onshore (Fig. 6), including a portion of the seismic zone D, showing relatively higher seismic energy release. Similarly, the Meilin Fault block, located at the southeastern boundary of our study area, covers seismic zone C and also exhibits relatively higher seismic energy release. The combination of significant accumulated seismic moment release and notable slip rate deficits suggests that despite frequent seismic activity, geological strain has not been fully relieved, increasing the likelihood of larger earthquakes in the future. However, note that not all segments of the Tainan Fault block and the Meilin Fault block are situated in areas with high seismic energy release, so any specific conclusions should be deferred until more solid evidence emerges.

The role of the deformation front in seismogenic processes

As delineated in literature, the DF represents the leading edge of a fold-thrust belt in western Taiwan (e.g., Liu et al. 1997; Huang et al. 2004; Han et al. 2017; Yu 2004). According to this conceptual framework, one would anticipate a prevalence of thrust faulting earthquakes along the eastern flank of the DF, while normal faulting earthquakes should be more common on the western side. Nevertheless, our observations deviate from this expected pattern. Specifically, as shown in Figs. 5 and S10–12, we discern a dominance of normal faulting and strike-slip faulting events near both the offshore and inland segments of the DF, respectively. Moreover, only a few well-constrained thrust faulting events occurred in the vicinity of the inland DF. This distinctive distribution pattern of focal mechanism solutions may be ascribed to the intensified collision between the EP and the PSP in SW Taiwan. Under the pronounced east–west compression resulting from the collision, the recurrent occurrence of normal faults may be hindered, instead manifesting as pre-existing weakness zones that become activated as reverse faults or strike-slip faults (e.g., Yang et al. 2016; Ruh and Vergés 2018; Chin et al. 2019). However, the activation mechanism is not well understood and warrants further study in detail, as it will provide crucial insights for earthquake hazard assessment.

Conclusions

We used 28-year earthquake data to accurately relocate hypocenters and determine focal mechanism solutions bracketing the 2017 Tainan earthquake sequence along the DF from onshore to offshore SW Taiwan. This extensive data set allowed us to understand better the long-term spatiotemporal variation in seismic activity and deformation pattern, which ultimately leads to characterizing five distinctive seismogenic structures in this high seismic potential area.

Remarkably, following the 2017 Tainan earthquake, seismic events primarily concentrated to the west of the DF and migrated northeastward. We propose that the offshore portion of the DF serves as a boundary, demarcating an area to the west of the DF, where seismic activity is primarily dominated by the flexural stress induced by the subducted EP. This pivotal observation may furnish the critical constraints for estimating the maximum magnitude of potential future earthquakes offshore SW Taiwan. As for the northwestward migration of seismic activity, the underlying mechanism remains unclear and will be the subject of our upcoming research endeavors.

Further examination unveiled that the areas with the highest cumulative seismic moment release were located near the surface trace of the DF rather than along known faults. This observation indicates the non-uniform distribution of seismic strain accumulation within the study area. In light of the debate surrounding whether the seismic strain release inherently possesses the potential for large earthquakes or conversely diminishes such likelihood, it is necessary to further comprehensively study the relationship between spatial–temporal distributions of seismic strain and seismic activity and the DF. In any case, it would be prudent to incorporate the DF into the seismic hazard assessments.

In addition, we identified serval earthquakes with the *P*-axis orientations parallel to the strike of the Taiwan orogen, which may provide new evidence to support the presence of collision-induced lateral compression within the subduction termination zone of southern Taiwan.

Acknowledgements

We thank the technical staff at the Central Weather Administration of Taiwan for their contributions in picking phase arrivals and P-wave first motion as well as maintaining the seismic networks. Special thanks to Chien-Hsin Chang, Chu-Wei Ho, Che-Wei Liao, and Tzu-Yi Yang for assembling earthquake data for this study. We acknowledge Yi-Wei Lin for offering the modified VELEST code, Kuan-Ting Chen for compiling the fault data from the Geological Survey and Ming Management Agency, Ministry of Economic Affairs, R.O.C., and Song-Chuen Chen for providing data of the deformation front. We are also grateful to Editor Ruey-Juin and two anonymous reviewers for suggestions that improved the manuscript. The Generic Mapping Tools (Wessel et al. 2019) are used in plotting.

Author contributions

Wen-Nan Wu: conceptualization, methodology, and writing—original draft preparation; Jing-Yi Lin: discussion, writing—review and editing. Wen-Bin

Doo: discussion, writing—review, and editing. Chung-Liang Lo: discussion, writing—review and editing. Shu-Kun Hsu: discussion, writing—review and editing, and funding acquisition. All authors read and approved the final manuscript.

Funding
This study was financially supported by the National Science and Technology Council, Taiwan.

Availability of data and materials
The arrival time data are acquired from the Geophysical Database Management System (GDMS) of the Central Weather Administration of Taiwan (https://gdms.cwa.gov.tw/). The outcomes of this study are available from the corresponding author upon reasonable request.

Declarations

Competing interests
The authors declare that they have no known competing financial interests or personal relationships that could have appeared to influence the work reported in this paper.

Received: 19 February 2024 Accepted: 31 July 2024
Published online: 14 August 2024

References

Chamberlain CJ, Frank WB, Lanza F, Townend J, Warren-Smith E (2021) Illuminating the pre-, co-, and post-seismic phases of the 2016 M7. 8 Kaikōura earthquake with 10 years of seismicity. J Geophys Res: Solid Earth. https://doi.org/10.1029/2021JB022304

Chen Y-L, Shin T-C (1998) Study on the earthquake location of 3-D velocity structure in the Taiwan area. Meteor Bull 42:135–169

Chen W-P, Hung S-H, Tseng T-L, Brudzinski M, Yang Z, Nowack RL (2012) Rheology of the continental lithosphere: progress and new perspectives. Gondwana Res 21(1):4–18. https://doi.org/10.1016/j.gr.2011.07.013

Chen S-C, Hsu S-K, Wang Y, Chung S-H, Chen P-C, Tsai C-H, Liu C-S, Lin H-S, Lee Y-W (2014) Distribution and characters of the mud diapirs and mud volcanoes off southwest Taiwan. J Asian Earth Sci 92:201–214. https://doi.org/10.1016/j.jseaes.2013.10.009

Chen H-Y, Hsu Y-J, Ikuta R, Tung H, Tang C-H, Ku C-S, Su H-H, Jian P-R, Ando M, Tsujii T (2022) Strain partitioning in the southern ryukyu margin revealed by seafloor geodetic and seismological observations. Geophys Res Lett. https://doi.org/10.1029/2022GL098218

Chin S-J, Lin J-Y, Yeh Y-C, Kuo-Chen H, Liang C-W (2019) Seismotectonic characteristics of the Taiwan collision-Manila subduction transition: the effect of pre-existing structures. J Asian Earth Sci 173:113–120. https://doi.org/10.1016/j.jseaes.2019.01.014

Ching K-E, Rau R-J, Johnson KM, Lee J-C, Hu J-C (2011) Present-day kinematics of active mountain building in Taiwan from GPS observations during 1995–2005. J Geophys Res: Solid Earth. https://doi.org/10.1029/2010JB008058

Doo W-B, Hsu S-K, Lo C-L, Chen S-C, Tsai C-H, Lin J-Y, Huang Y-P, Huang Y-S, Chiu S-D, Ma Y-F (2015) Gravity anomalies of the active mud diapirs off southwest Taiwan. Geophys J Int 203(3):2089–2098. https://doi.org/10.1093/gji/ggv430

Essing D, Poli P (2022) Spatiotemporal evolution of the seismicity in the Alto Tiberina fault system revealed by a high-resolution template matching catalog. J Geophys Res: Solid Earth. https://doi.org/10.1029/2022JB024845

Han W-C, Liu C-S, Chi W-C, Chen L, Lin C-C, Chen S-C (2017) Westward advance of the deformation front and evolution of submarine canyons offshore of southwestern Taiwan. J Asian Earth Sci 149:6–19. https://doi.org/10.1016/j.jseaes.2017.07.001

Hanks TC, Kanamori H (1979) A moment magnitude scale. J Geophys Res 84:2348–2350. https://doi.org/10.1029/JB084iB05p02348

Hardebeck JL, Shearer PM (2003) Using S/P amplitude ratios to constrain the focal mechanisms of small earthquakes. Bull Seismol Soc Am 93(6):2434–2444. https://doi.org/10.1785/0120020236

Hatch RL, Abercrombie RE, Ruhl CJ, Smith KD (2020) Evidence of aseismic and fluid-driven processes in a small complex seismic swarm near Virginia City, Nevada. Geophys Res Lett. https://doi.org/10.1029/2019GL085477

Hicks SP, Rietbrock A, Ryder IMA, Lee C-S, Miller M (2014) Anatomy of a megathrust: the 2010 M8.8 Maule, Chile earthquake rupture zone imaged using seismic tomography. Earth Planet Sci Lett 405:142–155. https://doi.org/10.1016/j.epsl.2014.08.028

Hsu Y-J, Ando M, Yu S-B, Simons M (2012) The potential for a great earthquake along the southernmost Ryukyu subduction zone. Geophys Res Lett 39:L14302. https://doi.org/10.1029/2012GL052764

Huang C-Y, Wu W-Y, Chang C-P, Tsaob S, Yuan PB, Lin C-W, Xia K-Y (1997) Tectonic evolution of accretionary prism in the arc-continent collision terrane of Taiwan. Tectonophysics 281(1–2):31–51. https://doi.org/10.1016/S0040-1951(97)00157-1

Huang C-Y, Yuan PB, Lin C-W, Wang TK, Chang C-P (2000) Geodynamic processes of Taiwan arc-continent collision and comparison with analogs in Timor, Papua New Guinea, Urals, and Corsica. Tectonophysics 325:1–21. https://doi.org/10.1016/S0040-1951(00)00128-1

Huang S-T, Yang K-M, Hung J-H, Wu J-C, Ting H-H, Mei W-W, Hsu S-H, Lee M (2004) Deformation front development at the northeast margin of the Tainan Basin, Tainan-Kaohsiung area, Taiwan. Mar Geophys Res 25(1):139–156. https://doi.org/10.1007/s11001-005-0739-z

Huang H-H, Wu Y-M, Song X, Chang C-H, Lee S-J, Chang T-M, Hsieh H-H (2014) Joint Vp and Vs tomography of Taiwan: implications for subduction-collision orogeny. Earth Planet Sci Lett 392:177–191. https://doi.org/10.1016/j.epsl.2014.02.026

Husen S, Hardebeck J (2011) Understanding seismicity catalogs and their problems. Commun Online Resour Stat Seism Anal. https://doi.org/10.5078/corssa-55815573

Jian PR, Tseng TL, Liang WT, Huang PH (2018) A new automatic full-waveform regional moment tensor inversion algorithm and its applications in the Taiwan area. Bull Seism Soc Am 108(2):573–587. https://doi.org/10.1785/0120170231

Kao H, Shen S-SJ, Ma K-F (1998) Transition from oblique subduction to collision: earthquakes in the southernmost Ryukyu arc-Taiwan region. J Geophys Res: Solid Earth 103(B4):7211–7229. https://doi.org/10.1029/97JB03510

Kilb D, Hardebeck JL (2006) Fault parameter constraints using relocated earthquakes: a validation of first-motion focal-mechanism data. Bull Seismol Soc Am 96(3):1140–1158. https://doi.org/10.1785/0120040239

Kissling E, Ellsworth WL, Eberhart-Phillips D, Kradolfer U (1994) Initial reference models in local earthquake tomography. J Geophys Res: Solid Earth 99:19635–19646. https://doi.org/10.1029/93JB03138

Kuo-Chen H, Wu FT, Roecker SW (2012) Three-dimensional P velocity structures of the lithosphere beneath Taiwan from the analysis of TAIGER and related seismic data sets. J Geophys Res: Solid Earth 117(B6):B06306. https://doi.org/10.1029/2011JB009108

Lin Y-W (2013) Structure of the subduction zone south of Taiwan constrained by OBS data. National Taiwan University, Taipei City

Lin G (2018) The source-specific station term and waveform cross-correlation earthquake location package and its applications to California and New Zealand. Seismol Res Lett 89(5):1877–1885. https://doi.org/10.1785/0220180108

Lin G, Okubo PG (2016) A large refined catalog of earthquake relocations and focal mechanisms for the Island of Hawai'i and its seismotectonic implications. J Geophys Res: Solid Earth 121(7):5031–5048. https://doi.org/10.1002/2016JB013042

Lin G, Shearer P (2005) Tests of relative earthquake location techniques using synthetic data. J Geophys Res: Solid Earth 110:B04304. https://doi.org/10.1029/2004JB003380

Lin J-Y, Wu W-N (2012) Spatio-temporal distribution of seismic moment release near the source area of the 2011 Tohoku-Oki earthquake. Earth, Planet Sp 64:1067–1075. https://doi.org/10.5047/eps.2012.04.006

Lin C-W, Liu Y-C, Chou P-S, Lin Y-H (2021) Recent development of active fault investigations of Taiwan. Bull Centr Geol Surv 34:1–40

Liu C-S, Huang IL, Teng LS (1997) Structural features off southwestern Taiwan. Mar Geol 137(3):305–319. https://doi.org/10.1016/S0025-3227(96)00093-X

Lo C-L, Doo W-B, Kuo-Chen H, Hsu S-K (2017) Plate coupling across the northern Manila subduction zone deduced from mantle lithosphere buoyancy. Phys Earth Planet Inter 273:50–54. https://doi.org/10.1016/j.pepi.2017.10.001

Mousavi SM, Ellsworth WL, Zhu W, Chuang LY, Beroza GC (2020) Earthquake transformer - an attentive deep-learning model for simultaneous earthquake detection and phase picking. Nat Commun 11(1):3952

Rau R-J, Lee J-C, Ching K-E, Lee Y-H, Byrne TB, Chen R-Y (2012) Subduction-continent collision in southwestern Taiwan and the 2010 Jiashian earthquake sequence. Tectonophysics 578:107–116. https://doi.org/10.1016/j.tecto.2011.09.013

Ross ZE, Rollins C, Cochran ES, Hauksson E, Avouac J-P, Ben-Zion Y (2017) Aftershocks driven by afterslip and fluid pressure sweeping through a fault-fracture mesh. Geophys Res Lett 44(16):8260–8267. https://doi.org/10.1002/2017GL074634

Ruh JB, Vergés J (2018) Effects of reactivated extensional basement faults on structural evolution of fold-and-thrust belts: insights from numerical modelling applied to the Kopet Dagh Mountains. Tectonophysics 746:493–511. https://doi.org/10.1016/j.tecto.2017.05.020

Sandiford D, Craig TJ (2023) Plate bending earthquakes and the strength distribution of the lithosphere. Geophys J Int 235(1):488–508. https://doi.org/10.1093/gji/ggad230

Sandwell DT, Smith WHF (1997) Marine gravity anomaly from Geosat and ERS 1 satellite altimetry. J Geophys Res: Solid Earth 102(B5):10039–10054. https://doi.org/10.1029/96JB03223

Tsai M-C, Yu S-B, Shin T-C, Kuo K-W, Leu P-L, Chang C-H, Ho M-Y (2015a) Velocity field derived from Taiwan continuous GPS array (2007–2013). Terr Atmos Ocean Sci 26(5):527–556. https://doi.org/10.3319/tao.2015.05.21.01(t)

Tsai M-C, Yu S-B, Shin T-C, Kuo K-W, Leu P-L, Chang C-H, Ho M-Y (2015b) Velocity field derived from Taiwan continuous GPS array (2007–2013). Terr Atmos Ocean Sci 26:527. https://doi.org/10.3319/tao.2015.05.21.01(t)

Vidale JE, Shearer PM (2006) A survey of 71 earthquake bursts across southern California: exploring the role of pore fluid pressure fluctuations and aseismic slip as drivers. J Geophys Res: Solid Earth 111:B05312. https://doi.org/10.1029/2005JB004034

Wang S-Y, Hsu S-K, Yeh Y-C (2019) Earthquake-related structures beneath the southernmost portion of the Ryukyu Arc and forearc. Geophys Res Lett 46(7):3717–3725. https://doi.org/10.1029/2019GL082121

Wessel P, Luis JF, Uieda L, Scharroo R, Wobbe F, Smith WHF, Tian D (2019) The generic mapping tools version 6. Geochem Geophys Geosyst 20(11):5556–5564. https://doi.org/10.1029/2019GC008515

Wu W-N, Yen Y-T, Hsu Y-J, Wu Y-M, Lin J-Y, Hsu S-K (2017) Spatial variation of seismogenic depths of crustal earthquakes in the Taiwan region: implications for seismic hazard assessment. Tectonophysics 708:81–95. https://doi.org/10.1016/j.tecto.2017.04.028

Wu W-N, Lo C-L, Doo W-B, Lin J-Y, Hsu S-K (2021) Seismogenic structure along the deformation front off SW Taiwan revealed by the aftershocks of the 2017 Tainan near-shore earthquake with ocean bottom seismometers. Tectonophysics 815:228995. https://doi.org/10.1016/j.tecto.2021.228995

Yang K-M, Rau R-J, Chang H-Y, Hsieh C-Y, Ting H-H, Huang S-T, Wu J-C, Tang Y-J (2016) The role of basement-involved normal faults in the recent tectonics of western Taiwan. Geol Mag 153(5–6):1166–1191. https://doi.org/10.1017/S0016756816000637

Yu H-S (2004) Nature and distribution of the deformation front in the Luzon Arc-Chinese continental margin collision zone at Taiwan. Mar Geophys Res 25(1):109–122. https://doi.org/10.1007/s11001-005-0737-1

Yu S-B, Chen H-Y, Kuo L-C (1997) Velocity field of GPS stations in the Taiwan area. Tectonophysics 274:41–59. https://doi.org/10.1016/S0040-1951(96)00297-1

Zhu G, Yang H, Yang T, Zhang G (2023) Along-strike variation of seismicity near the extinct mid-ocean ridge subducted beneath the Manila Trench. Seismol Res Lett 94(2A):792–804. https://doi.org/10.1785/0220220304

Publisher's Note